Draft version August 11, 2025
Typeset using LaTeX default style in AASTeX631

Gravitational lensing by a spiral galaxy I: the influence from bar's structure to the flux ratio anomaly

Xikai Shan,[1] Yunpeng Jin,[2] and Shude Mao[2]

[1]Department of Astronomy, Tsinghua University, Beijing 100084, China
[2]Department of Astronomy, Westlake University, Hangzhou 310030, Zhejiang Province, China

ABSTRACT

Gravitational lens flux ratio anomalies are a powerful probe of small-scale mass structures within lens galaxies. These anomalies are often attributed to dark matter subhalos, but the baryonic components of the lens can also play a significant role. This study investigates the impact of galactic bars, a common feature in spiral galaxies, on flux ratio anomalies. We conduct a systematic analysis using a sample of 21 barred galaxies from the high-resolution Auriga cosmological simulations. First, we model the projected mass distribution of these galaxies with the Multi-Gaussian Expansion (MGE) formalism. This method creates smooth, realistic lens potentials that preserve the primary bar structure while reducing numerical noise. We then perform strong lensing simulations and quantify the flux ratio anomalies by measuring their deviation from the theoretical cusp-caustic relation, denoted as $R_{\rm cusp}$. To characterize the structural properties of the bars, we use a Fourier decomposition of the surface mass density. For instance, the $m = 2$ mode quantifies the bar's strength, while the $m = 4$ mode measures the strength of its boxy or peanut shape. Our primary finding is a strong, statistically significant correlation between the magnitude of the flux ratio anomaly and the strength of the higher-order even Fourier modes. Specifically, the strengths of the boxy/peanut ($m = 4$) and hexapole ($m = 6$) components show an exceptionally tight correlation with $R_{\rm cusp}$ (Spearman $r > 0.95$), particularly for edge-on projections. This demonstrates that flux ratio anomalies are highly sensitive to the complex, non-axisymmetric features of galactic bars. We conclude that the flux ratio anomaly can be an indicator of a galactic bar's presence. Failing to account for a bar's complex morphology can lead to a misinterpretation of the lensing signature, potentially causing an overestimation of the dark matter subhalo population. This work underscores the necessity of including realistic baryonic structures in strong lensing models of spiral galaxies.

Keywords: Gravitational lensing — Flux ratio anomaly — Spiral galaxy lensing — Substructure lensing

1. INTRODUCTION

Gravitational lensing is a powerful tool for probing the distribution of matter, from individual galaxies to massive clusters (Schneider et al. 1992; Blandford & Narayan 1992). In the strong lensing regime, multiple images of a background source are formed. The flux ratios between these images provide a direct test of the smoothness of the foreground lens's gravitational potential (Mao & Schneider 1998). When the observed fluxes deviate from the predictions of a simple, smooth lens model, this phenomenon is known as a "flux ratio anomaly". Such anomalies point to the existence of additional mass structures that perturb the lens potential on small scales.

These anomalies have several potential origins. First, they can be caused by perturbations from dark matter subhalos within the main lens galaxy. This idea was first proposed by Mao & Schneider (1998) and has been studied extensively with theoretical models (Metcalf & Madau 2001; Dalal & Kochanek 2002) and high-resolution N-body

xk_shan@mail.bnu.edu.cn

shude.mao@westlake.edu.cn

cosmological simulations (Xu et al. 2009, 2010, 2013). Second, microlensing by the dense field of stars in the lens galaxy can contribute to the anomalies. This effect is particularly significant for lensed quasars observed at optical wavelengths (Irwin et al. 1989). Third, other structures along the line of sight, such as the external shear from the large-scale environment or intervening halos, can alter the observed fluxes (Suyu et al. 2010; Inoue & Takahashi 2012; Xu et al. 2012). A fourth potential origin is the lens galaxy's own baryonic structures, such as edge-on galactic disks (Hsueh et al. 2016, 2017, 2018).

In this study, we focus on the impact of baryonic structures on flux ratio anomalies. Specifically, we investigate the effect of galactic bars within spiral lens galaxies. Lensing by spiral galaxies offers several advantages over the more commonly studied elliptical lens systems. First, they enable a powerful combination of lensing constraints with kinematic data from the galaxy's stellar or gas components, often obtained with Integral Field Unit (IFU) spectroscopy. This synergy is crucial for breaking inherent degeneracies in dynamical studies, such as the disk-halo degeneracy (Maller et al. 2000; Dutton et al. 2011; Suyu et al. 2012). Second, the multiply-imaged configurations from these lenses serve as a high-resolution diagnostic tool, allowing us to probe the complex internal structures of spiral galaxies, including their spiral arms and central bars.

Although the predicted lensing rate by spiral galaxies was once considered low (Keeton & Kochanek 1998), a growing sample of these valuable systems is being discovered. This is thanks to ongoing and future large-scale surveys, such as the Euclid space telescope (Euclid Collaboration et al. 2025), the Vera C. Rubin Observatory (LSST Science Collaboration et al. 2009), and the Chinese Space Station Telescope (CSST) (Cao et al. 2024; CSST Collaboration et al. 2025). These discoveries are further enhanced by high-resolution observations with the James Webb Space Telescope (JWST), which can precisely characterize the lens and source properties (Caminha et al. 2022; Nightingale et al. 2025). This influx of data ensures that the sample of spiral galaxy lenses will continue to grow significantly.

This paper is the first in a series dedicated to exploring the influence of a key, yet under-investigated, structural component on flux ratio anomalies: the galactic bar. Photometric studies from optical to near-infrared wavelengths show that bars exist in more than half of nearby disk galaxies (Eskridge et al. 2000; Knapen et al. 2000; Marinova & Jogee 2007; Menéndez-Delmestre et al. 2007; Barazza et al. 2008; Sheth et al. 2008; Aguerri et al. 2009; Masters et al. 2011; Buta et al. 2015; Erwin 2018; Jin et al. 2025). As a significant non-axisymmetric mass component in the galaxy's center, the bar is a natural candidate for perturbing the lens potential. This study, therefore, addresses two fundamental questions: Can galactic bars produce measurable flux ratio anomalies? And conversely, can we use flux ratio anomaly measurements to infer the properties of bars in distant lensed galaxies? While previous work has explored the influence of angular multipoles on lensing observables (Evans & Witt 2003; Congdon & Keeton 2005; O'Riordan & Vegetti 2024; Paugnat & Gilman 2025), these studies have typically focused on the global structure of elliptical galaxies. Our work provides a new perspective by focusing specifically on the impact of bars within spiral lenses.

This paper is structured as follows. In Section 2, we introduce the suite of galaxy simulations used in our analysis. Section 3 details our lensing simulation and analysis methodology. We present our primary results in Section 4, followed by a summary and discussion of their implications in Section 5.

2. DATA PREPARATION

In this section, we describe the spiral galaxy data used in our strong lensing simulations (Section 2.1) and detail the method used to mitigate shot noise (Section 2.2).

2.1. *Auriga data projection*

The Auriga simulations are a suite of high-resolution, cosmological zoom-in simulations of thirty Milky Way-mass galaxies ($M_{200} \approx 1 - 2 \times 10^{12} M_\odot$). These simulations were performed with the moving-mesh code AREPO, achieving a baryonic mass resolution of $\sim 5 \times 10^4 M_\odot$ and a dark matter resolution of $\sim 3 \times 10^5 M_\odot$. The adaptive gravitational softening length reaches ~ 370 pc. The simulations incorporate a comprehensive galaxy formation model that accounts for star formation, supernova (Type Ia/II) feedback, chemical evolution, active galactic nucleus (AGN) feedback, magnetic fields, radiative cooling, and a uniform UV background. This model was calibrated to match key observables, such as the stellar mass-halo mass relation.

For this study, we use a subset of 21 barred galaxies from the full sample of thirty, following the classification in Blázquez-Calero et al. (2020). We use the $z = 0$ snapshots and place the lens galaxies at a redshift of $z_l = 0.5$ and the background source at $z_s = 1.0$.

The first step in our simulation is to create a two-dimensional projected mass density map for each lens galaxy. We achieve this by mapping the simulation particles onto a 2D grid using a standard Smoothed Particle Hydrodynamics (SPH) kernel (Monaghan 1992). During this step, we apply an adaptive smoothing technique to reduce shot noise from the discrete particles while preserving the primary bar structure. The smoothing length for each particle is set by the distance to its 640 nearest neighbors, with a maximum value capped at 1 kpc. While this initial smoothing affects the projected structure, it does not bias our final analysis. As detailed later, our method for quantifying flux ratio anomalies inherently accounts for the smoothing scale.

Figure 1 shows the projection of a representative Auriga galaxy (Au 10). The x and y axes are the spatial coordinates in kiloparsecs (kpc). The left and right columns display the galaxy from face-on and edge-on viewing angles, respectively. The color scale indicates the dimensionless convergence, κ, which is the two-dimensional mass density scaled by the critical surface density, $\Sigma_{\rm crit} = \frac{c^2}{4\pi G}\frac{D_{\rm s}}{D_{\rm l}D_{\rm ls}}$. The white lines are isodensity contours.

As seen in the figure, a bar structure is clearly visible in the galaxy's center, especially in the side-on projection. However, the isodensity contours are also irregular and asymmetric. These features arise from a combination of residual shot noise and physical substructures within the galaxy. To isolate the influence of the bar on flux ratio anomalies, we must mitigate these small-scale fluctuations. This ensures that any measured anomaly is driven primarily by the bar's structure, not by other factors. Therefore, we use the Multi-Gaussian Expansion (MGE) fitting method to create a smoothed representation of the galaxy.

2.2. *Multi gaussian fitting*

To address the presence of shot noise and small-scale fluctuations in the simulated convergence maps, we utilize a MGE fitting technique (Cappellari 2002). This method involves modeling the projected mass density, $\kappa(R', \theta')$, as a superposition of several concentric, two-dimensional Gaussian functions:

$$\kappa\left(R', \theta'\right) = \sum_{j=1}^{N} \frac{\kappa_j}{2\pi\sigma_j'^2 q_j'} \exp\left[-\frac{1}{2\sigma_j'^2}\left(x_j'^2 + \frac{y_j'^2}{q_j'^2}\right)\right] \tag{1}$$

In the two dimensional plane, (R', θ') is the polar coordinates. The coordinates (x_j', y_j') are Cartesian coordinates, given by $x_j' = R' \sin(\theta' - \psi_j)$ and $y_j' = R' \cos(\theta' - \psi_j)$. The parameters for each Gaussian are:

- κ_j: The central convergence of the j-th component.
- σ_j': The dispersion along the major axis.
- q_j': The axial ratio.

The bottom panel of Figure 1 displays the MGE fitting results for the Auriga galaxy (Au 10). Compared with the direct SPH projection in the upper panel, the isodensity contours (white curves) from the MGE fit are smoother and more symmetric. More importantly, the central bar structure is clearly resolved.

Therefore, the MGE method effectively smooths the density distribution while preserving key bar structural features. Based on this result, we will construct the lensing system using only the two-dimensional density distribution obtained from the MGE fitting.

3. LENSING METHODOLOGY

3.1. *Lensing basic theory*

The lens equation for a single lens plane can be written as:

$$\mathbf{y} = \mathbf{x} - \boldsymbol{\alpha}(\mathbf{x}), \tag{2}$$

where $\mathbf{y}$ is the position of the source in the source plane, $\mathbf{x}$ is the corresponding image position in the lens plane, and $\boldsymbol{\alpha}(\mathbf{x})$ is the deflection angle. The critical quantity in this equation is the deflection angle, which is the gradient of the two-dimensional lensing potential $\psi(\mathbf{x})$:

$$\boldsymbol{\alpha}(\mathbf{x}) = \boldsymbol{\nabla}\psi(\mathbf{x}). \tag{3}$$

The potential is related to the convergence $\kappa(\mathbf{x})$ of the lens galaxy through the Poisson equation:

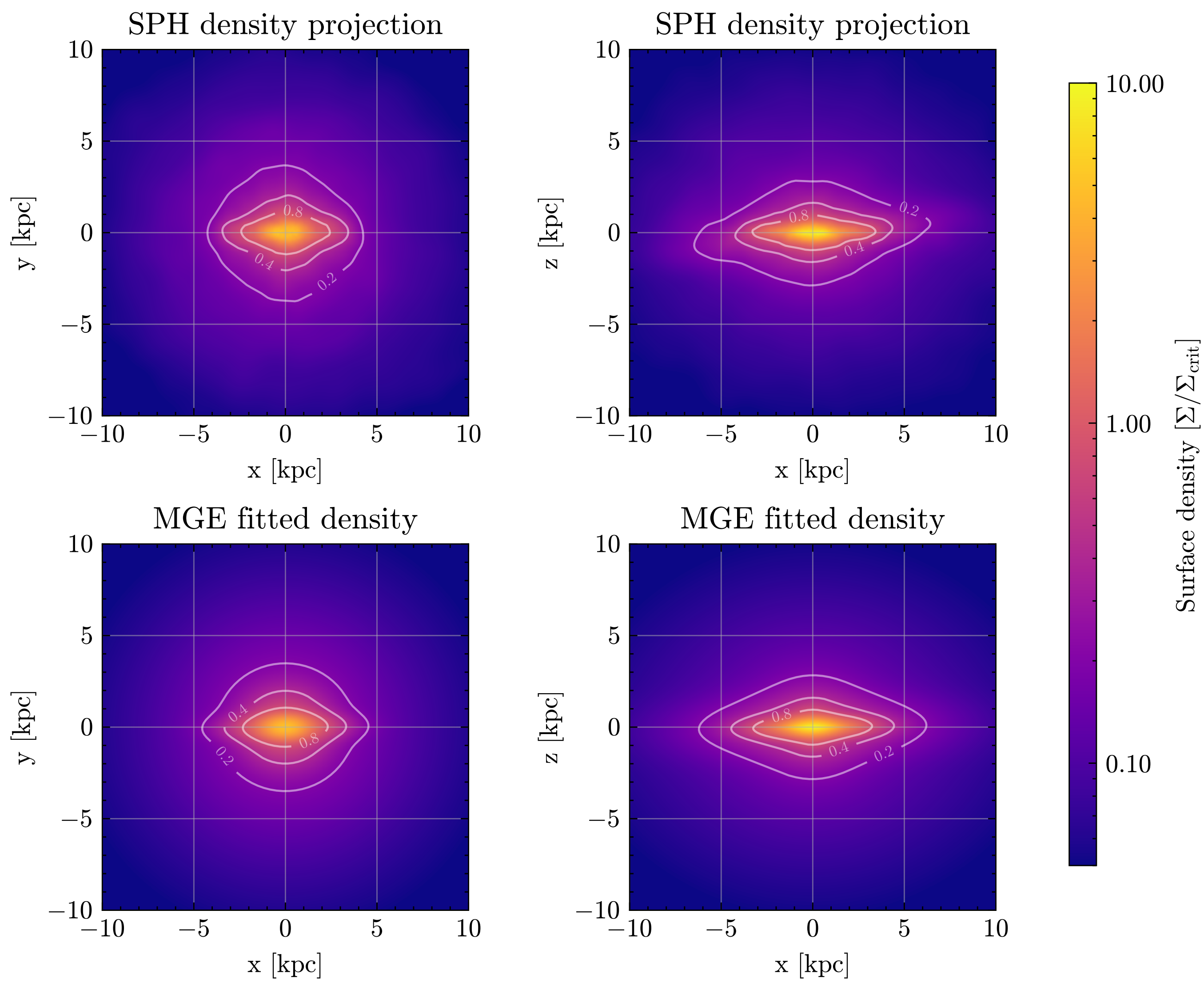

Figure 1. This figure displays the dimensionless surface density maps ($\kappa = \Sigma/\Sigma_{\rm crit}$) for Au 10 from the Auriga simulation. The columns show two different galactic projections: a face-on view (left) and an edge-on view with the bar oriented side-on (right). The top panels present the density maps derived from the direct projection using an SPH kernel, while the bottom panels show the corresponding maps reconstructed using a Multi-Gaussian Expansion (MGE) fit. In all panels, the color bar indicates the density level, with warmer colors denoting higher density regions, and the white lines represent iso-density contours.

$$\nabla^2 \psi(\mathbf{x}) = 2\kappa(\mathbf{x}). \tag{4}$$

As established in Section 2, the convergence map has already been generated. The next critical step is to solve Eq. (4) to derive the lensing potential. We achieve this using a standard Fast Fourier Transform (FFT) method. The convergence map has a resolution of 0.01 kpc, which is substantially smaller than the typical size of a galactic bar (a few kpc), and a boundary of 20 kpc, corresponding to approximately 0.1 R_{200}. This choice represents a balance between precision (resolution effect) and accuracy (boundary effect) under the constraints of current computational resources. Although the truncation of the density map can introduce external shear, the shear amplitude is only on the order of 10^{-2} at this truncation radius. Therefore, we neglect this effect on the flux ratio anomaly measurement (Van de Vyvere et al. 2020). Additionally, the finite resolution of the density map affects the accuracy of magnification calculations, particularly in regions of very high magnification. These regions occur in the proximity of critical curves, where the image magnification, μ, is inversely proportional to its distance, δr, from the critical curve (i.e., $\mu \propto 1/\delta r$;

Schneider et al. (1992)). Given the resolution of our density map, we, therefore, impose an artificial threshold on the magnification, setting the maximum value to 100.

Once the lensing potential $\psi(\mathbf{x})$ is obtained, it can be substituted into Eq. (3) and Eq. (2) to solve for the image positions $\mathbf{x}$ for a specified source position $\mathbf{y}$. After locating all images, their corresponding magnifications, μ, are calculated by using:

$$\mu = \frac{1}{(1-\kappa)^2 - \gamma^2}, \tag{5}$$

where κ is the convergence and γ is the shear magnitude. These quantities are defined in terms of the second partial derivatives of the lensing potential $\psi_{ij} = \frac{\partial^2 \psi}{\partial x_i \partial x_j}$. The convergence is given by:

$$\kappa = \frac{1}{2}(\psi_{11} + \psi_{22}), \tag{6}$$

and the shear is characterized by two components, γ_1 and γ_2:

$$\gamma_1 = \frac{1}{2}(\psi_{11} - \psi_{22}), \tag{7}$$

$$\gamma_2 = \psi_{12} = \psi_{21}. \tag{8}$$

The shear magnitude is the combination of these two components $\gamma = \sqrt{\gamma_1^2 + \gamma_2^2}$.

3.2. *Cusp caustic relation*

In a strong gravitational lensing system, a source located near a caustic cusp produces three images on one side of the lens center. For a smooth lens potential, the magnifications of these three images are expected to satisfy the theoretical cusp caustic relation:

$$R_{\rm cusp} \equiv \frac{|\mu_A + \mu_B + \mu_C|}{|\mu_A| + |\mu_B| + |\mu_C|} \to 0 \quad (\Delta\beta \to 0), \tag{9}$$

where $\Delta\beta$ represents the distance from the source to the caustic cusp, and μ_A, μ_B, and μ_C are the magnifications of the three respective images.

Since the source-caustic distance, $\Delta\beta$, is not directly observable in a strong lensing system, a proxy relationship between $R_{\rm cusp}$ and the opening angle of the images, $\Delta\phi$, is employed. The opening angle is defined as the angle formed by the two outermost images, with the vertex at the lens center. This angle can be measured directly from the lensed image, and a smaller opening angle indicates that the source is closer to the caustic cusp. Consequently, the opening angle $\Delta\phi$ serves as a key observable for testing the cusp caustic relation.

However, the assumption of a smooth lens potential is an idealization, as lens galaxies typically contain substructures. These substructures perturb the gravitational potential and can violate the cusp caustic relation, leading to a phenomenon known as a "flux ratio anomaly" (Mao & Schneider 1998). In this paper, we utilize this relationship to quantify the influence of a galactic bar on the observed flux ratio anomalies.

4. RESULT

In this section, we present the results of our lensing system construction and investigate the correlation between the strength of the angular complexity in the bar region and two key metrics: the caustic area—a proxy for lensing probability—and flux-ratio anomalies.

4.1. *Lens Mapping for Auriga Halos*

Here, we illustrate the construction of the lensing system based on the Auriga simulated data. Figure 2 displays the results for Au 10, which is the same halo shown in Figure 1. We set the lens redshift to $z_l = 0.5$ and the source redshift to $z_s = 1.0$.

The top panels of Figure 2 show the caustics for different projection angles: face-on (left), edge-on with the side-on bar (right). The x and y axes represent the source plane coordinates in units of arcseconds. The red curves denote the tangential caustics, which produce four images, while the blue curves are the radial caustics (also known as cuts), which produce two images. The gray shaded regions near the caustic cusps indicate the source sampling areas, where we randomly placed 10^4 sources at each cusp.

The bottom panels show the corresponding $\mathrm{R_{cusp}}$ values, as defined in Eq. (9), as a function of the opening angle, $\Delta\phi$, of the image triplets, with the vertex at the lens position. The red open circles represent the sample points. To ensure that the sources are located as close to the cusp as possible, we only include results with an opening angle of less than 90°. Through this analysis, we find that sources near the minor cusps (the regions along the x-axis) readily produce triplet images with opening angles of less than 90°. Conversely, for positions near the major cusps (the regions along the y-axis), only a few points generate triplet images with opening angles smaller than 90°. This is because the major cusp is influenced by the underlying smooth elliptical disk or bar structure. At the resolution of our lensing convergence map, we are unable to simulate a source sufficiently close to the major cusp to generate images with such a small opening angle. Therefore, in the bottom panels and the subsequent analysis, we only consider the results from the minor cusp regions.

From the lower panels, it is evident that $\mathrm{R_{cusp}}$ is approximately linearly proportional to the opening angle $\Delta\phi$. Based on this property, we fit the data points with a linear curve. As shown, the blue fitted curve accurately represents the data. To quantify the effect of the bar across different scenarios consistently, we use the value of $\mathrm{R_{cusp}}$ at an opening angle of 60° to represent the flux ratio anomaly. This value can be obtained from the yellow cross curves.

4.2. *The description of the the angular complexity strength in the bar region*

In this section, we establish a quantitative framework for characterizing the structural properties of galactic bars. Our primary objective is to develop the necessary tools to test the proposed connection between bar strength and flux ratios anomaly.

While the concept of a "strong" or "weak" bar is intuitive, its quantification is not trivial. A variety of metrics have been proposed in the literature, ranging from the bar's projected axial ratio to functions of the tangential forces exerted on galactic material (Combes & Sanders 1981; Block et al. 2001). In this work, we adopt the Fourier decomposition method, a powerful technique for isolating non-axisymmetric structures, as detailed in Athanassoula & Misiriotis (2002). This approach allows us to measure the strength of the bar and its associated higher-order components, such as boxy and peanut-shaped morphologies.

The method begins by decomposing the galaxy's deprojected surface density, $\Sigma(r,\theta)$, into a series of Fourier modes within concentric radial annuli:

$$A_m(r) = \frac{1}{\pi}\int_0^{2\pi} \Sigma(r,\theta)e^{-im\theta}\,d\theta, \quad m = 0, 1, 2, \ldots \tag{10}$$

Here, $A_m(r)$ is the complex Fourier amplitude of the m-th component at radius r. The $m = 0$ mode, $A_0(r)$, corresponds to the azimuthally averaged surface density at that radius. The physical interpretation of other modes are also well-established: The even-numbered modes trace the primary bisymmetric structures characteristic of barred galaxies.

- **The $m = 2$ mode:** This is the dominant mode in a barred galaxy and directly measures the primary strength of the bar itself (Athanassoula & Misiriotis 2002).
- **The $m = 4$ mode:** This mode quantifies the bar's deviation from a pure elliptical shape. A significant $m = 4$ component is the classic signature of the boxy or peanut-shaped bulges that are often the result of vertical buckling instabilities in the bar (Combes & Sanders 1981; Athanassoula 2005a).
- **The $m = 6$ mode:** A non-zero $m = 6$ component can trace hexapole (six-fold) distortions in the central regions or the presence of an inner ring. It can also be associated with the bases of spiral arms emerging from the ends of the bar (Athanassoula & Misiriotis 2002).

The odd-numbered modes describe asymmetric features within the galaxy. While generally weaker than the even modes in mature, isolated barred galaxies, they can provide important physical insights.

- **The $m = 1$ mode:** This mode measures the galaxy's "lopsidedness", corresponding to a large-scale asymmetry where the nucleus is displaced relative to the outer disk isophotes. Such features are often attributed to tidal interactions with companion galaxies or asymmetries in the accretion of gas or dark matter (Rix & Zaritsky 1995; Zaritsky & Rix 1997).

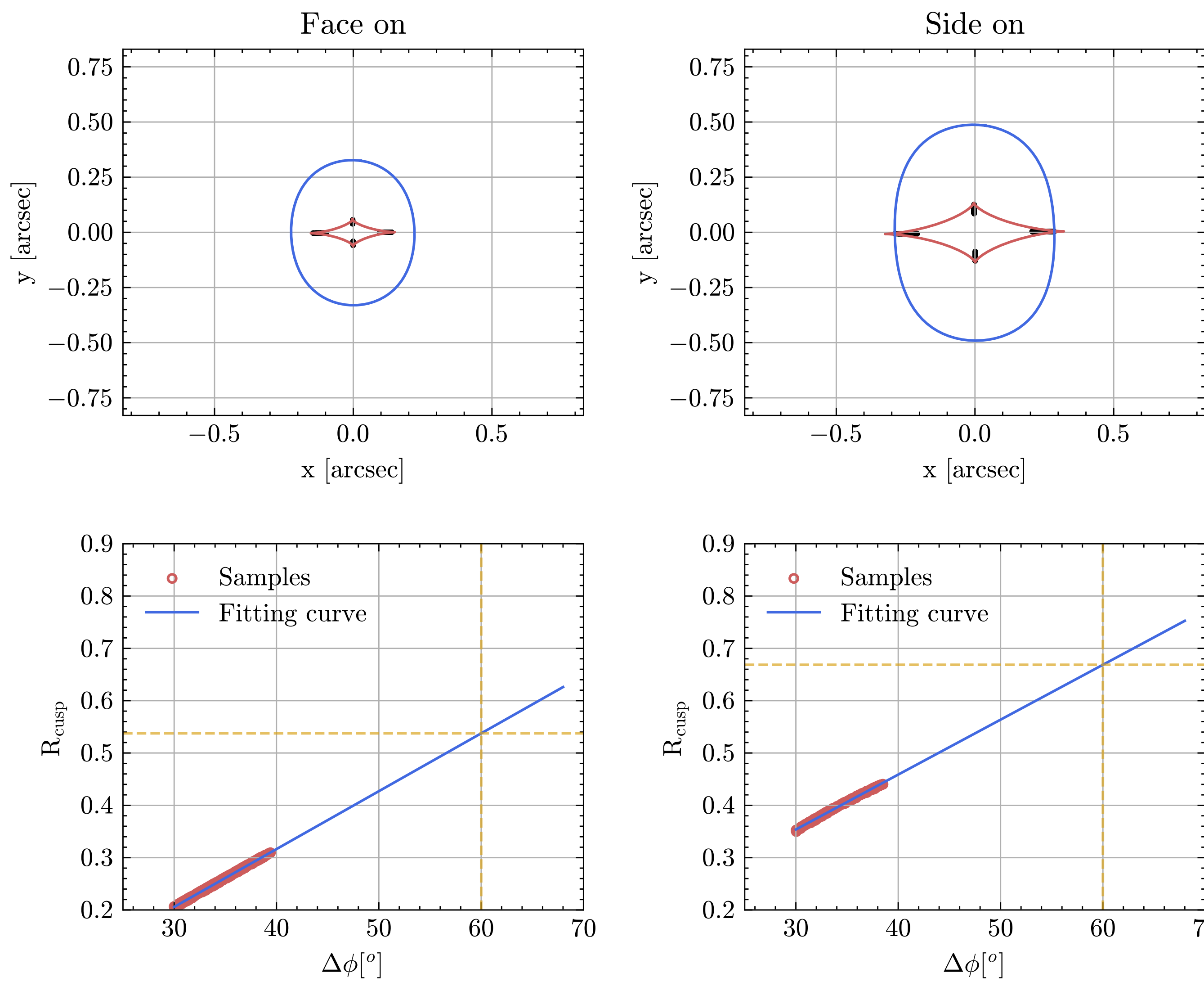

Figure 2. The top panels illustrate the tangential (diamond-shaped) and radial (elliptical-shaped) caustics. The columns correspond to different galaxy projections: the left panel shows a face on view and the right panel shows an edge on view with a side on bar. The gray dots near the caustic cusps represent the sampled source positions, with 10^4 points used for each position. The lower panels plot the cusp caustic relation, R_{cusp} (defined in Eq. 9), as a function of the opening angle, $\Delta\phi$. In these plots, the red open circles denote the data from the sampled points, while the solid blue curves represent the best-fit linear polynomials. The yellow cross in each lower panel indicates the value of R_{cusp} at an opening angle of 60°.

- **The $m = 3$ and $m = 5$ modes:** These higher-order odd modes trace more complex asymmetries, such as triangular distortions ($m = 3$) (Athanassoula 1984).

To quantify the relative contribution of each high order component ($m = 1, 2, 3, \ldots$), we normalize its amplitude by the background $A_0(r)$. we then define the maximum value of the ratio $A_m(r)/A_0(r)$ across all radii as a global measure of the strength of the m-th order structural component.

Finally, it is worth noting that to ensure the decomposition results reflect the bar's influence, we limit the calculation to the bar's region, as defined in Table 1 of Blázquez-Calero et al. (2020).

Figure 3 presents the radial profiles of the normalized Fourier amplitudes, $\mathrm{A_m/A_0}$, for Au 10, shown from two distinct projections: face-on (left column) and side-on (right column). The top row displays the odd-order components ($m = 1, 3, 5$), while the bottom row shows the even-order components ($m = 2, 4, 6$).

Three primary trends are immediately apparent from the figure. First, the even-order Fourier components consistently exhibit significantly larger amplitudes than their odd-order counterparts. This is expected, as the galaxy's structure is dominated by the bar, a feature with strong bisymmetry ($m = 2$). The power in higher even modes ($m = 4, 6$) and all odd modes, which trace less prominent structural features or asymmetries, is naturally lower. Within each modes (even or odd), the amplitudes systematically decrease as the order m increases. This reflects the physical reality that the majority of the galaxy's structural power resides in large-scale components (like the bar itself), whereas the power in smaller-scale, higher-angular-frequency details diminishes progressively. (Athanassoula & Misiriotis 2002).

Second, the radial location of the peak amplitude systematically shifts to larger radii as the Fourier order m increases. This trend is a direct consequence of the spatial distribution of the physical structures that each mode traces. The $m = 2$ mode captures the primary bar structure, with its peak amplitude occurring where the bar is most dominant—typically in the main body of the bar, inside its full length. In contrast, higher-order modes, such as $m = 4$ and $m = 6$, trace features like boxy/peanut isophotes and hexapole distortion. These structures are prominent toward the ends of the bar. Consequently, the radii where these higher-order modes have their maximum contribution are located further out than the peak of the primary $m = 2$ mode.

A third notable trend is the systematic increase in the peak amplitudes of both odd and even-order modes when a galaxy is viewed edge-on views with side-on bars versus face-on. This phenomenon is a direct consequence of projection effects tied to the bar's intrinsic triaxial structure; as a body that is elongated within the disk plane but vertically thin, its projection appears as a more highly concentrated feature when viewed side on (see Figure 1 for an illustration). This maximizes the density contrast between the bar and the azimuthally averaged background. Consequently, the relative amplitudes of all non-axisymmetric Fourier modes, represented by the ratio $\mathrm{A_m}/\mathrm{A_0}$, are enhanced.

4.3. *The correlation between the strength of the bar and lensing phenomenon*

In this section, we investigate the correlation between the angular complexity in the bar region and two key metrics: the caustic area—a proxy for lensing probability—and flux-ratio anomalies.

We begin by examining Au 10 as a representative case study. The top panel of Figure 2 shows that, the tangential and radial caustics area is significantly larger for the side-on projection than for the face-on view.

This trend is consistent with the structural properties of the bar itself. As shown in Figure 3, the peak amplitudes of the Fourier modes are also systematically larger when the bar is viewed side-on. The correspondence between these two independent measurements suggests a direct correlation between the strength of the bar's non-axisymmetric features and the resulting lensing caustic area.

To robustly investigate these correlations, we analyze a sample of 21 barred galaxies from the Auriga simulations, identical to the sample used by Blázquez-Calero et al. (2020). Each galaxy is viewed from two distinct projection angles, resulting in a total of 42 test cases. The results are presented in Figure 4, which plots the tangential (upper panel) and radial (lower panel) caustic areas against the peak amplitude of the Fourier modes, $\max(\mathrm{A_m}/\mathrm{A_0})$. The statistical significance of these relationships is quantified using the Spearman rank correlation coefficient (r) and the corresponding p-value, both of which are annotated in each panel.

A clear distinction emerges between the even- and odd-order Fourier components. The even modes ($m = 2, 4, 6$) exhibit stronger correlations with caustic area than the odd-order modes, as evidenced by their larger correlation coefficients. Furthermore, within both the even and odd sets, the correlation strength systematically increases with the mode number, m. The hexapole ($m = 6$) mode, in particular, displays the strongest correlation among all components tested. Finally, the p-values for all six correlations are extremely low ($p < 0.001$), indicating that the observed trends are statistically significant.

These results establish a direct connection between the size of the tangential caustic and the strength of higher-order angular structural components in the region of galaxy bar. Since these non-axisymmetric modes are all physical manifestations of the underlying galactic bar, this finding implies a more fundamental relationship: galaxies hosting stronger, more structurally complex bars are expected to produce larger tangential caustic areas and, consequently, have a higher probability of generating strong lensing events.

In contrast, the radial caustic area exhibits a different behavior. Here, the $m = 2$ mode, representing the primary strength of the bar, shows the strongest correlation. This suggests that the size of the radial caustic is predominantly sensitive to the bar's fundamental strength, rather than the higher-order angular structures that influence the tangential caustic.

We then investigate the correlation between the strength of the angular complexity in the bar region and the flux ratio anomaly, defined here as $R_{\mathrm{cusp}}(\Delta\phi)$ evaluated at a cusp opening angle of $\Delta\phi = 60°$. Figure 5 presents these

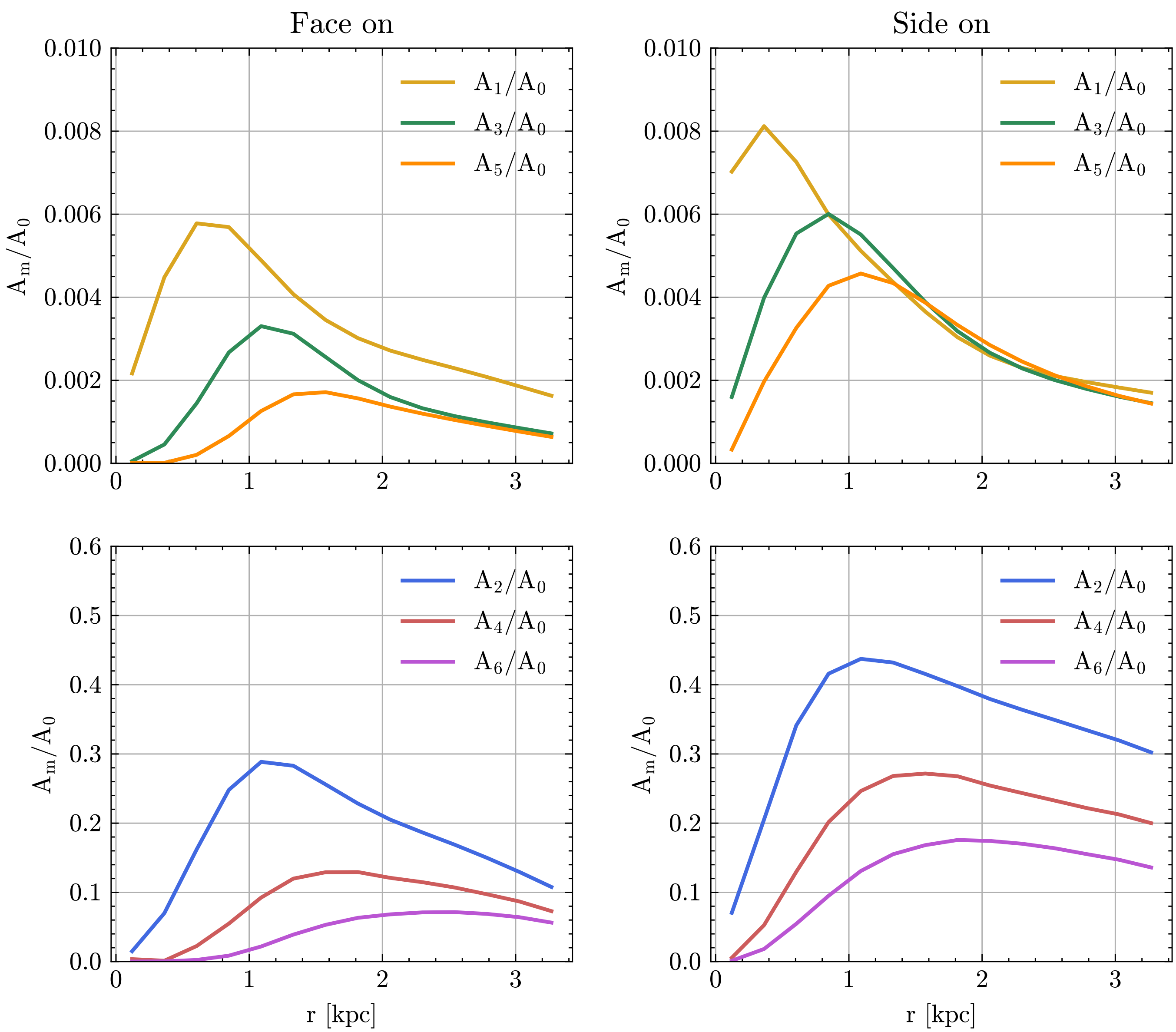

Figure 3. Profiles of the relative Fourier amplitudes, $\mathrm{A_m/A_0}$, as a function of radius in kiloparsecs (kpc). The left and right columns correspond to different galaxy projections: a face-on view and an edge-on view with the bar is side on, respectively. The top row displays the odd Fourier components ($m = 1, 3, 5$), while the bottom row displays the even components ($m = 2, 4, 6$). Within each panel, different colored lines distinguish the Fourier modes as indicated by the legend.

relationships, with each panel dedicated to a specific Fourier mode amplitude, $\max(\mathrm{A_m/A_0})$, plotted on the x-axis. Different viewing projections are distinguished by color (red for face-on and blue for side-on) and the Spearman correlation coefficient (r) and corresponding p-value are shown in the legend.

The results reveal several clear trends. First, the even-order components ($m = 2, 4, 6$) consistently exhibit stronger correlations with $R_{\mathrm{cusp}}(60^{\circ})$ than the odd-order components. Furthermore, a systematic pattern emerges within both the even and odd modes: as the Fourier order m increases, the correlation with the flux ratio anomaly becomes stronger. This trend is particularly striking for the side-on projections of the $m = 4$ and $m = 6$ modes, which capture the boxy/peanut and hexapole structures, respectively. In these cases, the correlation is exceptionally strong, with coefficients of $r > 0.95$ and p-values on the order of 10^{-3}.

This extremely tight correlation indicates a robust, physical connection between flux ratio anomalies and the presence of these higher-order features. Consequently, an unexpectedly high value of R_{cusp} may imply that the bar has

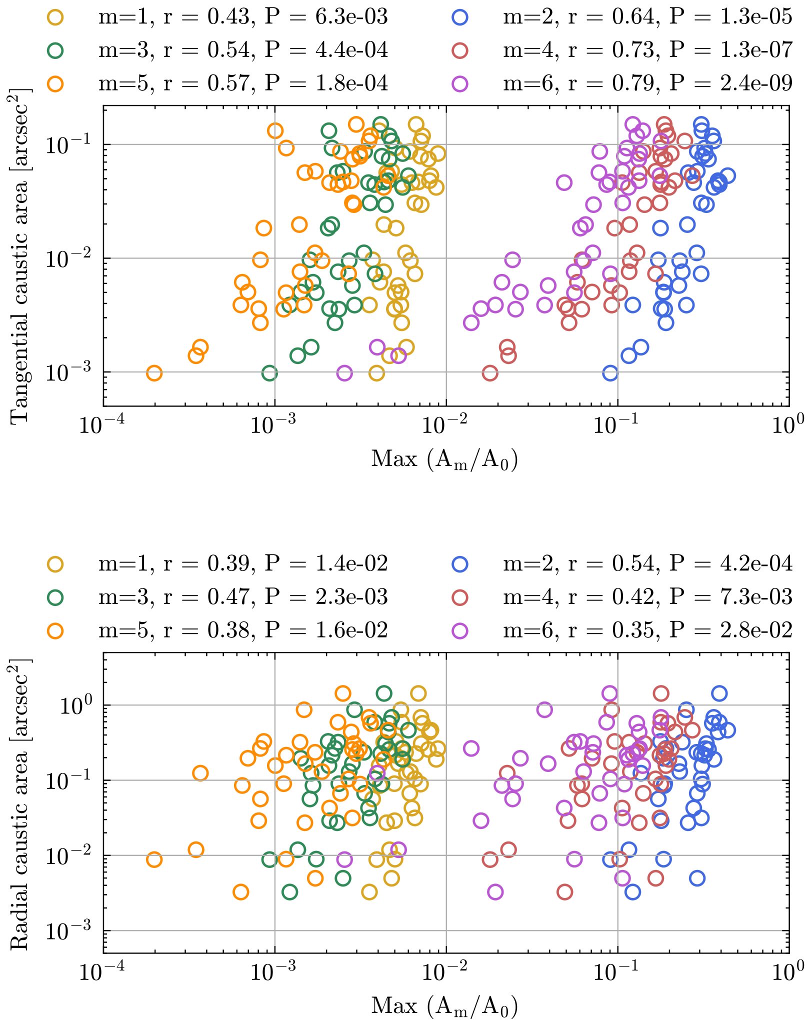

Figure 4. Correlations between the peak Fourier amplitudes, max(A_m/A_0), and the lensing caustic area. The top and bottom panels show the results for the tangential and radial caustic areas, respectively. Each color represents a different Fourier component, from $m = 1$ to $m = 6$. The legend provides the Spearman correlation coefficient (r) and the associated p-value for each component, indicating the statistical significance of the correlation.

boxy/peanut and hexapole components in lensed galaxies. The presence of these structures is a key diagnostic for understanding galaxy evolution, as they are widely considered to be signposts of secular evolution processes, driven by the bar, which rearrange disk material and build up the central components of galaxies over cosmic time (Kormendy & Kennicutt 2004; Athanassoula 2005b).

In addition to the dominant correlations found for the $m = 4$ and $m = 6$ modes, we also observe moderate correlations between $R_{\rm cusp}(60^\circ)$ and the peak amplitudes of the $m = 2, 3,$ and 5 components, primarily in the face-on projection. For these modes, the Spearman coefficient (r) can exceed 0.5 with p-values below 0.03. This suggests that an anomalously high value of $R_{\rm cusp}$ may also imply the presence of a strong bar (from the $m = 2$ correlation) as well as triangular ($m = 3$) and pentagonal ($m = 5$) distortions within the bar of a lensing galaxy. In contrast, for any remaining modes, we do not find a statistically significant correlation between their strength and the $R_{\rm cusp}$ measurement.

In conclusion, the flux ratio anomaly is most strongly correlated with the strength of even, higher-order structures, specifically the boxy/peanut (A_4) and hexapole (A_6) components, rather than with the odd or lower-order modes. This finding indicates that the flux ratio anomaly is particularly sensitive to small-scale, high-angular-frequency perturbations in the gravitational potential. It can therefore serve as a valuable and quantitative proxy for the strength of these complex, higher-order morphological features in lensed galaxies.

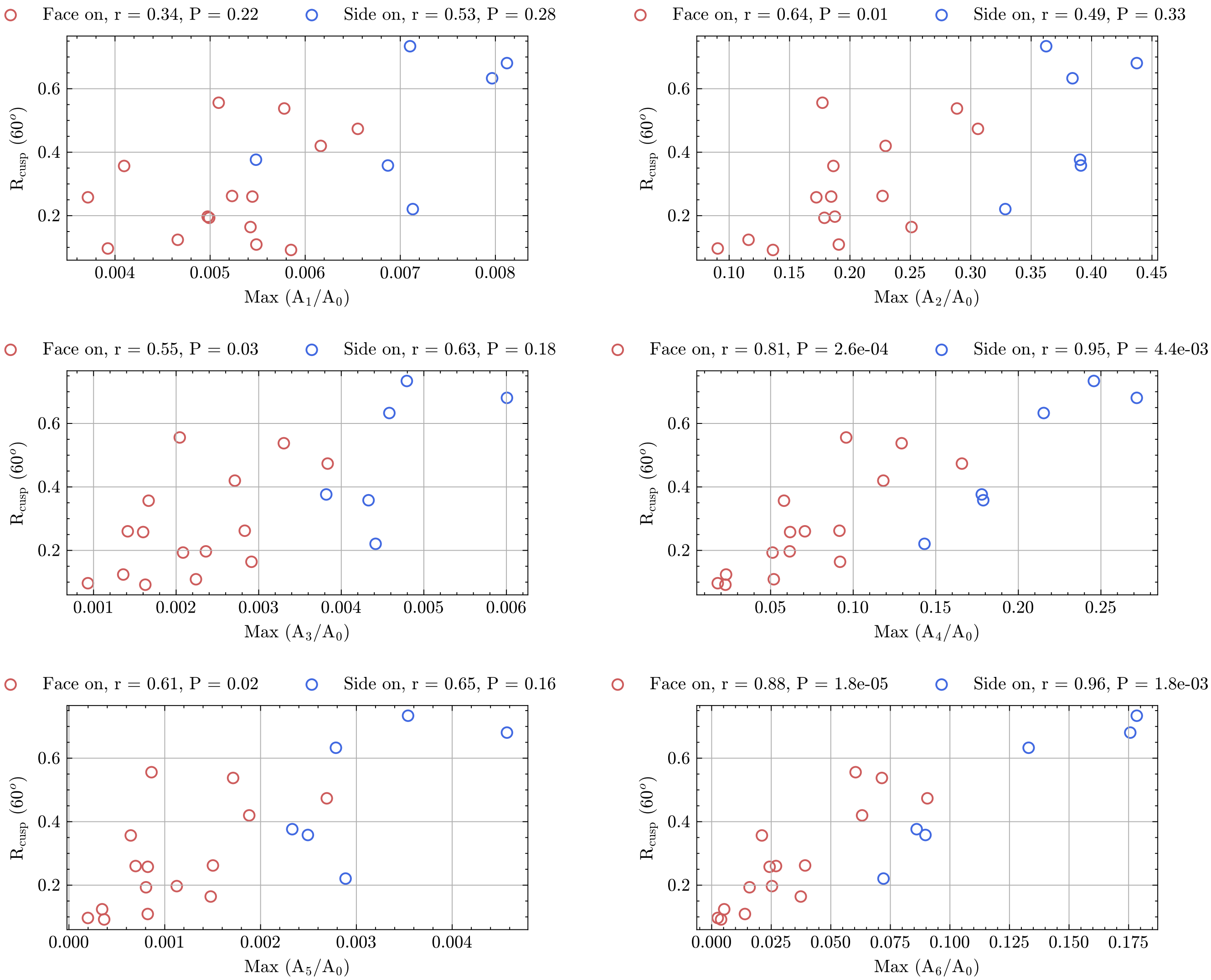

Figure 5. Correlations between the cusp-caustic flux ratio, $R_{\rm cusp}(60^{\circ})$, and the peak amplitude of six different Fourier components, $\max(A_{\rm m}/A_0)$. The results are shown for two different galaxy orientations: face-on (red) and edge-on with the bar viewed side-on (blue). The legend in each panel provides the Spearman correlation coefficient (r) and the associated p-value, indicating the statistical significance of the correlation.

5. CONCLUSION AND DISCUSSION

Galactic bars are ubiquitous features in spiral galaxies, observed in approximately 65% of the local disk galaxy population (Sheth et al. 2008). With the advent of large-scale surveys such as Euclid and the upcoming Chinese Space Station Telescope (CSST), the sample of galaxy-galaxy strong lensing systems with spiral lens galaxies is expected to grow substantially. Concurrently, advancements in Integral Field Unit (IFU) spectroscopy and kinematic modeling provide an independent means of mapping the mass distribution of these lens galaxies. The combination of kinematic data with strong lensing constraints offers a powerful method for breaking the well-known degeneracy between disk and halo components (Maller et al. 2000; Trott & Webster 2002; Dutton et al. 2011; Suyu et al. 2012), leading to more accurate mass reconstructions.

In this work, we have investigated the influence of galactic bar structures on the cusp-caustic relationship, which is a direct probe of flux ratio anomalies. Our analysis is based on strong lensing simulations of 21 barred spiral galaxies selected from the Auriga project, as detailed in Blázquez-Calero et al. (2020). To isolate the impact of the bar, we developed a methodology to mitigate noise from numerical simulations (e.g., shot noise) and astrophysical substructures (e.g., dark matter subhalos). This was achieved by fitting the projected surface mass density, initially rendered with a Smoothed Particle Hydrodynamics (SPH) kernel, using the MGE method. As illustrated in Figure 1, the MGE-fitted surface density is significantly smoother and more symmetric than the direct SPH projection, ensuring that our measured flux ratio anomalies are predominantly influenced by the large-scale asymmetry of the galactic bar.

Figure 2 shows the lensing simulation result for the lens galaxy shown in Figure 1. The caustic area is notably larger for an edge-on projection compared to a face-on view, a direct consequence of the higher projected surface mass density in the edge-on case. Furthermore, we found that the cusp relation, $R_{\rm cusp}$, is nearly linearly proportional to the opening angle of the triplet images. We leverage this linearity to define a standardized metric for the flux ratio anomaly, $R_{\rm cusp}(60^{\circ})$, derived from a linear fit to the cusp relation.

To characterize the bar's structure, we employed a Fourier decomposition of the MGE-derived surface density. The strengths of the various morphological components were quantified by the peak amplitude of their respective Fourier modes, A_m/A_0, as shown in Figure 3. This analysis highlighted three key trends: (1) The galaxy's morphology is dominated by even-order modes, particularly the $m = 2$ bar component. (2) The peak amplitudes of higher-order modes ($m > 2$) occur at larger radii, tracing features such as boxy/peanut-shaped isophotes. (3) An edge-on projection enhances the amplitudes of all modes by increasing the density contrast of the bar against the galactic disk.

We established statistically significant correlations between the bar's structural components and its lensing properties. The caustic areas, a proxy for the strong lensing cross-section, show distinct dependencies on different Fourier modes (Figure 4). The tangential caustic area correlates most strongly with higher-order even modes (specifically, the $m = 6$ hexapole component), indicating that structurally complex bars produce larger tangential caustics. In contrast, the radial caustic area is most sensitive to the primary bar strength ($m = 2$). It is well-established that the caustic area is primarily determined by the central density of the lens galaxy (Schneider et al. 1992). Our findings, therefore, imply a physical connection: galaxies with higher central densities tend to host stronger and more structurally complex bars. We will investigate this connection in detail in our future work.

The central result of this paper is the strong, direct correlation between $\mathrm{R}_{\rm cusp}$ and the strength of the bar's different components. We find boxy/peanuts ($m = 4$) and hexapole ($m = 6$) components showing exceptionally tight relationships (Pearson's $r > 0.95$), particularly in edge-on projections. This demonstrates that flux ratio anomalies are most significantly influenced by high-frequency angular components, which are characteristic of complex bar structures.

In conclusion, this study—the first in a series—establishes that the higher-order structural components of galactic bars (e.g., boxy/peanut and hexapole features) are strongly correlated with flux ratio anomalies. This finding presents a critical implication for strong lensing studies: an observed flux ratio anomaly in a system with a spiral lens galaxy may not exclusively signify the presence of dark matter subhalos, but could instead be caused by the complex structure of the galactic bar itself. Consequently, our results underscore the necessity of incorporating realistic, morphologically complex bar components into strong lensing models to accurately interpret observations. Strong lensing techniques may also be used to detect bars at high redshifts (Trott et al. 2010).

This work is partly supported by the National Science Foundation of China (Grant No. 12133005). X.S. acknowledges support from Shuimu Tsinghua Scholar Program (No. 2024SM199) and the China Postdoctoral Science Foundation (Certificate Number: 2025M773189).

REFERENCES

Aguerri, J. A. L., Méndez-Abreu, J., & Corsini, E. M. 2009, A&A, 495, 491, doi: 10.1051/0004-6361:200810931

Athanassoula, E. 1984, PhR, 114, 319, doi: 10.1016/0370-1573(84)90156-X

Athanassoula, E. 2005a, in American Institute of Physics Conference Series, Vol. 804, Planetary Nebulae as Astronomical Tools, ed. R. Szczerba, G. Stasińska, & S. K. Gorny (AIP), 333–340, doi: 10.1063/1.2146306

—. 2005b, MNRAS, 358, 1477, doi: 10.1111/j.1365-2966.2005.08872.x

Athanassoula, E., & Misiriotis, A. 2002, MNRAS, 330, 35, doi: 10.1046/j.1365-8711.2002.05028.x

Barazza, F. D., Jogee, S., & Marinova, I. 2008, ApJ, 675, 1194, doi: 10.1086/526510

Blandford, R. D., & Narayan, R. 1992, ARA&A, 30, 311, doi: 10.1146/annurev.astro.30.1.311

Blázquez-Calero, G., Florido, E., Pérez, I., et al. 2020, MNRAS, 491, 1800, doi: 10.1093/mnras/stz3125

Block, D. L., Puerari, I., Knapen, J. H., et al. 2001, A&A, 375, 761, doi: 10.1051/0004-6361:20010775

Buta, R. J., Sheth, K., Athanassoula, E., et al. 2015, ApJS, 217, 32, doi: 10.1088/0067-0049/217/2/32

Caminha, G. B., Suyu, S. H., Mercurio, A., et al. 2022, A&A, 666, L9, doi: 10.1051/0004-6361/202244517

Cao, X., Li, R., Li, N., et al. 2024, MNRAS, 533, 1960, doi: 10.1093/mnras/stae1865

Cappellari, M. 2002, MNRAS, 333, 400, doi: 10.1046/j.1365-8711.2002.05412.x

Combes, F., & Sanders, R. H. 1981, A&A, 96, 164

Congdon, A. B., & Keeton, C. R. 2005, MNRAS, 364, 1459, doi: 10.1111/j.1365-2966.2005.09699.x

CSST Collaboration, Gong, Y., Miao, H., et al. 2025, arXiv e-prints, arXiv:2507.04618, doi: 10.48550/arXiv.2507.04618

Dalal, N., & Kochanek, C. S. 2002, ApJ, 572, 25, doi: 10.1086/340303

Dutton, A. A., Brewer, B. J., Marshall, P. J., et al. 2011, MNRAS, 417, 1621, doi: 10.1111/j.1365-2966.2011.18706.x

Erwin, P. 2018, MNRAS, 474, 5372, doi: 10.1093/mnras/stx3117

Eskridge, P. B., Frogel, J. A., Pogge, R. W., et al. 2000, AJ, 119, 536, doi: 10.1086/301203

Euclid Collaboration, Walmsley, M., Holloway, P., et al. 2025, arXiv e-prints, arXiv:2503.15324, doi: 10.48550/arXiv.2503.15324

Evans, N. W., & Witt, H. J. 2003, MNRAS, 345, 1351, doi: 10.1046/j.1365-2966.2003.07057.x

Hsueh, J.-W., Despali, G., Vegetti, S., et al. 2018, MNRAS, 475, 2438, doi: 10.1093/mnras/stx3320

Hsueh, J. W., Fassnacht, C. D., Vegetti, S., et al. 2016, MNRAS, 463, L51, doi: 10.1093/mnrasl/slw146

Hsueh, J. W., Oldham, L., Spingola, C., et al. 2017, MNRAS, 469, 3713, doi: 10.1093/mnras/stx1082

Inoue, K. T., & Takahashi, R. 2012, MNRAS, 426, 2978, doi: 10.1111/j.1365-2966.2012.21915.x

Irwin, M. J., Webster, R. L., Hewett, P. C., Corrigan, R. T., & Jedrzejewski, R. I. 1989, AJ, 98, 1989, doi: 10.1086/115272

Jin, Y., Zhu, L., Tahmasebzadeh, B., et al. 2025, arXiv e-prints, arXiv:2505.02917, doi: 10.48550/arXiv.2505.02917

Keeton, C. R., & Kochanek, C. S. 1998, ApJ, 495, 157, doi: 10.1086/305272

Knapen, J. H., Shlosman, I., & Peletier, R. F. 2000, ApJ, 529, 93, doi: 10.1086/308266

Kormendy, J., & Kennicutt, Jr., R. C. 2004, ARA&A, 42, 603, doi: 10.1146/annurev.astro.42.053102.134024

LSST Science Collaboration, Abell, P. A., Allison, J., et al. 2009, arXiv e-prints, arXiv:0912.0201, doi: 10.48550/arXiv.0912.0201

Maller, A. H., Simard, L., Guhathakurta, P., et al. 2000, ApJ, 533, 194, doi: 10.1086/308641

Mao, S., & Schneider, P. 1998, MNRAS, 295, 587, doi: 10.1046/j.1365-8711.1998.01319.x

Marinova, I., & Jogee, S. 2007, ApJ, 659, 1176, doi: 10.1086/512355

Masters, K. L., Nichol, R. C., Hoyle, B., et al. 2011, MNRAS, 411, 2026, doi: 10.1111/j.1365-2966.2010.17834.x

Menéndez-Delmestre, K., Sheth, K., Schinnerer, E., Jarrett, T. H., & Scoville, N. Z. 2007, ApJ, 657, 790, doi: 10.1086/511025

Metcalf, R. B., & Madau, P. 2001, ApJ, 563, 9, doi: 10.1086/323695

Monaghan, J. J. 1992, ARA&A, 30, 543, doi: 10.1146/annurev.aa.30.090192.002551

Nightingale, J., Mahler, G., McCleary, J., et al. 2025, arXiv e-prints, arXiv:2503.08777, doi: 10.48550/arXiv.2503.08777

O'Riordan, C. M., & Vegetti, S. 2024, MNRAS, 528, 1757, doi: 10.1093/mnras/stae153

Paugnat, H., & Gilman, D. 2025, PhRvD, 111, 123014, doi: 10.1103/d14h-f5mn

Rix, H.-W., & Zaritsky, D. 1995, ApJ, 447, 82, doi: 10.1086/175858

Schneider, P., Ehlers, J., & Falco, E. E. 1992, Gravitational Lenses, doi: 10.1007/978-3-662-03758-4

Sheth, K., Elmegreen, D. M., Elmegreen, B. G., et al. 2008, ApJ, 675, 1141, doi: 10.1086/524980

Suyu, S. H., Marshall, P. J., Auger, M. W., et al. 2010, ApJ, 711, 201, doi: 10.1088/0004-637X/711/1/201

Suyu, S. H., Hensel, S. W., McKean, J. P., et al. 2012, ApJ, 750, 10, doi: 10.1088/0004-637X/750/1/10

Trott, C. M., Treu, T., Koopmans, L. V. E., & Webster, R. L. 2010, MNRAS, 401, 1540, doi: 10.1111/j.1365-2966.2009.15780.x

Trott, C. M., & Webster, R. L. 2002, MNRAS, 334, 621, doi: 10.1046/j.1365-8711.2002.05542.x

Van de Vyvere, L., Sluse, D., Mukherjee, S., Xu, D., & Birrer, S. 2020, A&A, 644, A108, doi: 10.1051/0004-6361/202038942

Xu, D. D., Mao, S., Cooper, A. P., et al. 2012, MNRAS, 421, 2553, doi: 10.1111/j.1365-2966.2012.20484.x

—. 2010, MNRAS, 408, 1721, doi: 10.1111/j.1365-2966.2010.17235.x

Xu, D. D., Sluse, D., Gao, L., et al. 2013, arXiv e-prints, arXiv:1307.4220, doi: 10.48550/arXiv.1307.4220

Xu, D. D., Mao, S., Wang, J., et al. 2009, MNRAS, 398, 1235, doi: 10.1111/j.1365-2966.2009.15230.x

Zaritsky, D., & Rix, H.-W. 1997, ApJ, 477, 118, doi: 10.1086/303692